K. A. Seffen[1]
Department of Engineering,
University of Cambridge,
Trumpington Street,
Cambridge CB2 1PZ, UK
e-mail: kas14@cam.ac.uk

S. V. Stott
Department of Engineering,
University of Cambridge,
Trumpington Street,
Cambridge CB2 1PZ, UK

Surface Texturing Through Cylinder Buckling

We consider the axial buckling of a thin-walled cylinder fitted onto a mandrel core with a prescribed annular gap. The buckling pattern develops fully and uniformly to yield a surface texture of regular diamond-shaped buckles, which we propose for novel morphing structures. We describe experiments that operate well into the postbuckling regime, where a classical analysis does not apply; we show that the size of buckles depends on the cylinder radius and the gap width, but not on its thickness, and we formulate simple relationships from kinematics alone for estimating the buckle proportions during loading. [DOI: 10.1115/1.4026331]

1 Introduction

In this paper, we complement the early work on cylindrical shell buckling by Horton and Durham [1]. They devised a novel experiment for enabling a well-developed buckle pattern over the entire shell, in order to quantify the effect of initial geometrical imperfections, which, at the time, was taken to be responsible for premature buckling loads. Under axial compression, a thin-walled tube tends to collapse after forming a locally buckled region at a random location on the shell, at a much lower load than predicted by a classical analysis. Attempts to reconcile matters for design purposes considered, for example, the introduction of knockdown factors applied to the theoretical load (a modern account is given in [2]). Horton and Durham adopted a different approach by repeating the experiment after placing a smaller, solid cylindrical mandrel inside the shell before loading. Local buckles can no longer grow unrestrained because their radial displacements are arrested by impingement on the mandrel, thereby allowing more buckles to form, which eventually accumulate into a diamondlike pattern over the entire cylinder. At this point, the mode-shape is uniform and complete, and matches the doubly-periodic form used in a linear stability analysis. Horton and Durham were then able to confirm the classical buckling load with the measured axial force, with excellent agreement between them when imperfections were minimal.

The mandrel in their work enabled the classical result to be "reached" in the sense of restabilizing the postbuckling response. The annular gap was set equal to the thickness of the shell in all experiments, for a single fixed geometry of cylinder. Once the fully buckled form was established, only the total number of buckles was recorded; the buckled geometry is evident in their photographs but the axial and circumferential wavelengths were not measured nor predicted because the buckling load, ultimately, does not depend on their values. This also highlights the incredible focus of time by many researchers (see, e.g., [3] for a brief historical review), upon reconciling the axial capacity to theory in the sense of loads, that a regular mode-shape underpinned the correlation to the classical load without needing to classify its properties. More recently, the question of buckle geometry was tackled by Hunt et al. [4] for ordinary cylinder buckling, who chose a short enough shell so that localized formation of buckles takes place over a significant proportion of the total height of shell. The mode-shape, which typically emerges as only one or two rings of periodic displacements, is deemed to be periodic in both directions, enabling Hunt et al. to adapt the familiar Koiter Circle approach [5], based upon double-periodicity for estimating the hoop-wise wave-number.

We are interested in characterizing the buckled geometry of Horton and Durham in a modern context, for promoting shape-changing, or "morphing," structures in new technologies reliant upon a controllable surface "texture," for example, haptic electronic displays, building facades with tunable thermodynamical properties, and aerodynamical surfaces that can switch from being smooth to rough, and back again. In this sense, the behavior must remain elastic well into the postbuckled regime, so we deal with very thin shells whose radius-to-thickness is greater than 1000, above the value of 800 used by Horton and Durham, and much higher than the typical upper limit of 500 for practical shells. Correspondingly, our cylinders resemble membrane tubes rather than shells and, because of such thinness, postbuckling is dominated by inextensible behavior, where a well-known, associated mode-shape is the "Yoshimura" pattern [6], with commensurate features observed here. We were originally focused on the torsional "wrinkling" of membranes wrapped around tubes without knowledge of Horton and Durham's work when we noticed a distinctive doubly-periodic buckled pattern after compressing the membrane ends. We decided to change our focus and concentrate on the axial case alone. There are also parallels with recent studies on the buckling of thin films connected to compliant substrates, where distinctive surface patterns are wrought by in-plane compressive stresses [7–9], where the substrate elastically restrains the out-of-plane deformations in the same way that the mandrel provides a "hard" constraint. Many results come from simulations, because experiments are notoriously difficult to arrange, whereas our patterns can be quickly observed with inherent uniformity by wrapping a thin sheet of paper loosely around a cardboard tube before compressing it by hand. Another related study concerns the "stamping" of initially constrained elastic plates by confining them further between rigid surfaces [10]. This shows, rather elegantly, the transition from a buckled state to a wrinkled state, depending on the level of confinement, and this inspires our procedure as follows.

Foremost, we are concerned with how the overall buckled shape performs when the initial annular gap between the shell and mandrel is varied. In particular, experiments show that the circumferential wavelength, viz. the number of circumferential buckles, appears to be governed only by the annular gap size and the radius of mandrel (or shell), and not its thickness nor axial length. This differs from the observations of Hunt et al., where, recall, no mandrel is present, and the choice of length must be contrived to fit with the expected buckle size. In our case, length does not matter because the mode-shape is restabilized by the mandrel and because inextensibility during postbuckling implies that the thickness does not influence matters provided it is small

enough. Furthermore, the number of circumferential buckles does not depend on the load. This empirical observation allows us to decouple our views of the buckle geometry along and around the cylinder and thence to treat them separately. The corresponding wavelengths are reasonably straightforward to deduce using the assumption of inextensibility because we may view them as the deformed loci of the shell in these directions, as if packaged according to geometrical constraints. This approach is novel in its kinematical basis; that we are able to deduce the loaded shape, albeit approximately, without solving for the nonlinear governing shell equations of deformation [11]. This study then concludes.

2 Experiments and Observations

Figure 1 shows a cylinder made of Mylar, a commercially available membrane material used by the aerospace industry for its resilience to fracture and tearing despite a thickness here of just 0.044 mm. The cylinder has a nominal radius of 30 mm after wrapping a flat sheet around a rigid aluminum tube. The tube remains in place to form an inner mandrel, which differs in radius from the Mylar by 1%. This gap is fashioned precisely by inserting a rodlike shim between the Mylar and the mandrel before joining the edges of the sheet along a narrow, overlapping seam of width typically less than 2% of the circumference, see Fig. 4(a) below. The shim is then removed so that the annular gap is free of obstruction, and the mandrel is slightly shorter so that only the Mylar cylinder is compressed by the end-plates. As expected, local buckles form first at random positions on the cylinder, Fig. 1, but each has a distinctive diamondlike shape depressed across its middle with edge ridges that eventually become highly creased. All diamonds are oriented with their axes of symmetry aligned to the axial and circumferential directions, and all have roughly the same size.

When the surface becomes entirely covered, the diamonds are approximately square and subdivided into a pair of triangular facets by a circumferential crease. The overall layout now resembles the well-known Yoshimura cylinder pattern [6] shown in Figs. 2(a) and 2(b). This pattern, which may be formed by folding a flat sheet, allows the cylinder to be compressed into a compact stack of plates inextensibly; there is no local stretching or compression of the material, only rotation about the hinge-lines. The facet geometry is not predisposed to a particular shape although many pictures show them as being equilateral, and Johnson et al. [12] recognized that different triangular shapes yield diverse collapse properties overall. Rotation about the creases in our Mylar

cylinders is not perfectly inextensible, because the creases are not singular lines, rather, they are ridges with additional concentrated features, see Figs. 2(c)–2(e). However, all tests develop the same facetted pattern, and these attempt to close during compression so that the diamonds are reduced in height. In doing so, each center is forced inwards, and the crease begins to form a distributed contact patch on the mandrel, evident in Fig. 1 and in close-up in Figs. 2(c)–2(e). All patches continue to grow in size even though the number of diamonds remains fixed; their height continues to decrease and their peripheral ridges become more pronounced. As the adherence increases, the axial capacity of the cylinder increases significantly due to the build-up of frictional resistance.

In general, we observe that the diamond buckles are larger when the initial gap is increased and when the cylinder is larger overall, and vice versa. The "mismatch" in radii between the cylinder and the mandrel, as well as their absolute sizes are key in determining the shape and number of buckles, but so is the uniformity of radius. Figure 3 indicates three differently-shaped mandrels: the standard cylindrical tube, a squashed cylinder that is approximately elliptical, and an airfoil-like section made by bending an aluminum plate around a standard NACA profile. The Mylar "sleeve" wrapped around each of them is made with the same degree of mismatch. As the local radius of curvature of the mandrel is reduced, so is the diamond width. This is most demonstrable in the third case, which has a highly-curved and textured leading edge feeding into the trailing, flatter part with diamonds merging across the width and growing in size up to fivefold.

Returning to cylindrical mandrels, we note that the buckled texture can be wrought easily by hand, and their circumferential properties quickly established. Later, we present results obtained in this way for cylinders fitted onto three mandrel sizes of 29.6, 31.6, and 63.5 mm for a range of mismatches. In order to extract accurate information, formal measurements are taken using an Instron tensometer, and the schematic setup is shown in Fig. 4(b). A single aluminum tube of radius 50 mm forms the mandrel, and a thin-walled, sliding collar at the top end allows the Mylar cylinder to be compressed while being supported radially. We ignore the shape over this short region because the annular gap is slightly different, and five cylinders were made in the same way as before, with mismatches in radii ranging from 2.4% to 9.9% by using different sizes of rod shim during manufacture.

During compression, a very different response is presented: local buckles accumulate into rings, which form successively along the length of cylinder. Once the pattern is fully formed, the buckles are typically nonuniformly sized axially, and sometimes

| (a) | (b) | (c) | (d) |
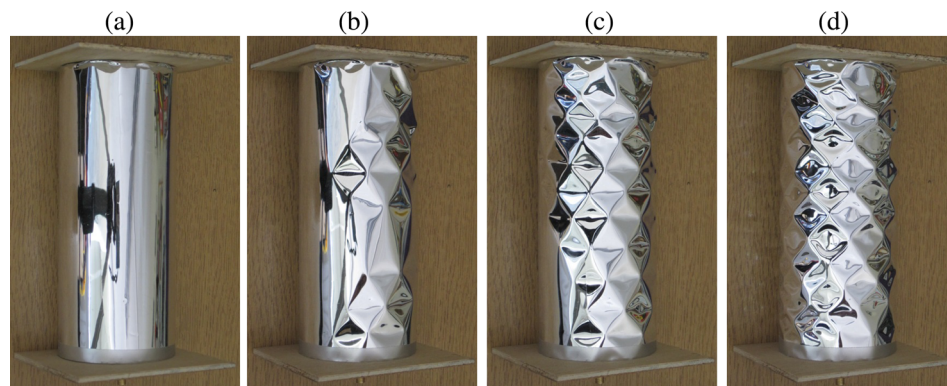
Fig. 1 Progressive formation of a surface texture during axial buckling of a thin-walled cylinder. (*a*) Initially, the cylinder is mounted as a close-fitting sleeve on a rigid cylindrical mandrel (not in view), and the wooden end pieces, or platens, are pushed together; a small axial gap allows the sleeve to compress without loading the mandrel. (*b*) Diamond-like buckles manifest locally at first, and their tendency to displace inwards is arrested by the mandrel, which allows their number to increase over the entire surface. (*c*) Further compression produces a high level of contact between the cylinder and mandrel. (*d*) The cylinder has length 150 mm and diameter 60 mm, and its radius differs from that of the mandrel by 1%. The material is Mylar with a thickness of 0.044 mm.
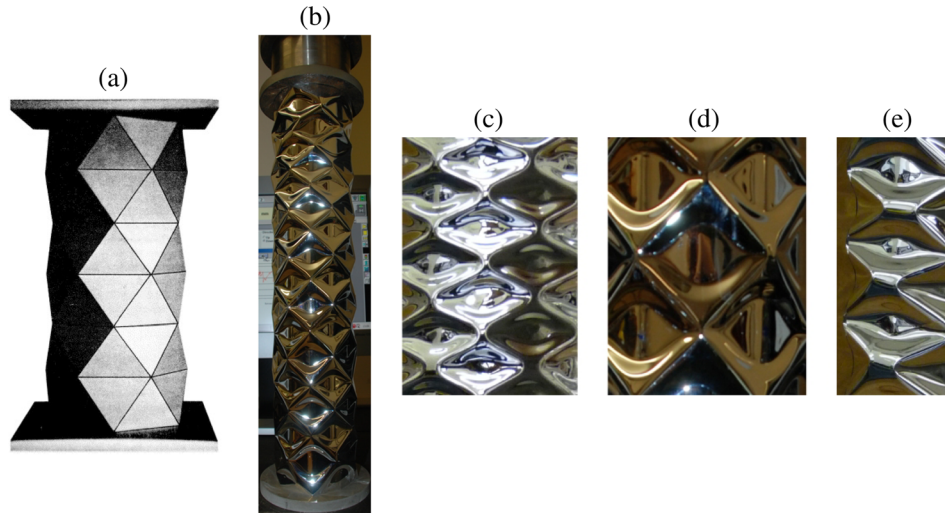
Fig. 2 (*a*) Yoshimura's facetted cylinder, created by folding a flat sheet along prescribed hinge lines, before joining the edges, courtesy of [6]. (*b*) Formal testing of our cylinders produces a distinctive Yoshimura pattern. (*c*)–(*e*) Close-up view of diamond buckle details for different cylinders. (*c*) The smallest mismatch gives ridges that curve and touch at adjacent corners. (*d*) A larger mismatch produces a more distinctive polygonal outline for each diamond, with significant adherence over the inner mandrel. (*e*) The largest mismatch produces adjacent ridges that tend to be separated. The features in (*c*)–(*e*) help to inform upon the simple circumferential mode-shapes presented in Fig. 8.
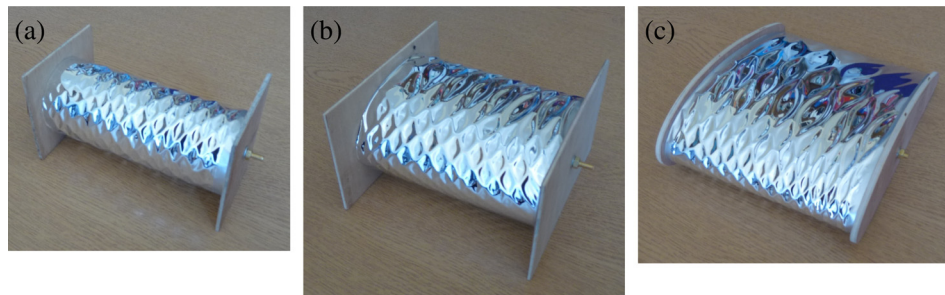

Fig. 3 Surface textures due to axial buckling of thin-walled tubes fitted onto three differently shaped mandrels of (*a*) circular, (*b*) elliptical, and (*c*) airfoil sections. Each shows that the buckle size is affected by the local radius of mandrel curvature. In (*a*), all are the same, whereas in (*b*) and (*c*), they become larger when the section becomes flatter, and vice versa. The wooden end-plates enable axial compression to be applied.

they do not form all the way along. Both effects are mainly due to the previous friction preventing the applied axial force from being transmitted equally along the length. This seems to be an artifact of the testing setup because of the precise way in which the force is applied. When the cylinders are compressed by hand by gripping their ends, there is less local constraint in view of these boundary conditions, and the pattern can form freely and uniformly. By running a hand over a compressed cylinder, we discovered that the buckles can be rendered uniform in size. When the cylinders are unloaded from this point, the response is uniform in this direction, because the cylinder expands radially, thereby relaxing contact, and hence lowering the internal friction. Attempts to lower the coefficient of friction by other means, for example, by spraying silicon lubricant onto the mandrel beforehand, proved fruitless. Thus, for a more consistent view of the buckled shape, we decided to record the unloading response for all five cylinders in this way, and Fig. 5 indicates the axial force versus the endwise displacement for unloading. At points in the profile, we also measured properties of the buckles, namely, their width, height, and their circumferential number, but it became clear that the behavior was dominated by two responsive modes, now described.

For the smallest mismatch, the buckles offload in unison by increasing in height together. The applied force reduces nonlinearly so that the overall stiffness decreases to the point where it approaches zero just before the original cylindrical shape is recovered. Over this final phase of unloading, buckles "pop" back individually, the stiffness rises sharply to a roughly linear value, and the force decreases to zero over an axial strain of 0.4%. On the other hand, buckles offload progressively for the largest mismatch, with rings of buckles opening up successively, and then increasing in height together and uniformly, with the rest of the cylinder remaining static. The force response throughout is given by small fluctuations about a mean value every time a static ring begins to open and become absorbed into the general restoration of shape. This phase resembles the force response of the foldable cylinders of Guest and Pellegrino [13], which were designed deliberately as collapse mechanisms. A final linear phase can also be observed as the force approaches zero.

The difference in both of these modes, is again, due to friction. A relatively smaller contact area within each buckle arises for smaller mismatches, and the frictional forces can be overcome everywhere so that the entire cylinder is capable of sliding against the mandrel. With larger mismatches, there is more contact and
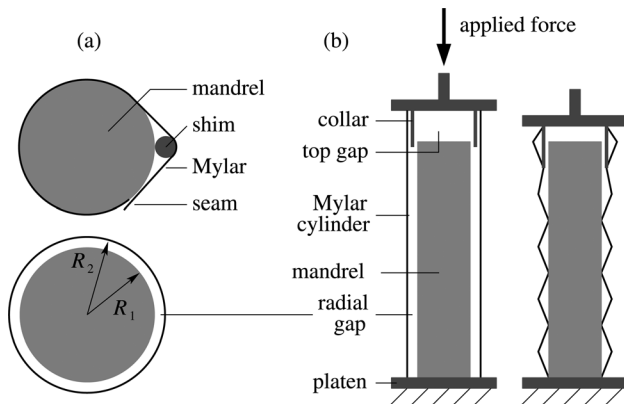
Fig. 4 (*a*) Manufacture of a cylinder by wrapping a flat Mylar sheet around a cylindrical mandrel. In order to create a precise annular gap, a rod is inserted as a shim to create extra circumferential length. A seam is created from a small overlapping joint. The shim is then removed to leave a slightly larger outer cylinder, where the mismatch in radii can be characterized by defining $\xi = (R_2/R_1) - 1$. For example, in one case tested later, the radii of the mandrel and the shim rod are 50 mm and 4.76 mm, respectively, giving $\xi = 2.4\%$. (*b*) Formal compression scheme using an Instron tensometer. A sliding collar is fitted to the top platen so that only the cylinder is compressed while the bulk of its surface is in contact with the mandrel. In all of these experiments, the mandrel has a radius of 50 mm, and is approximately 300 mm tall.
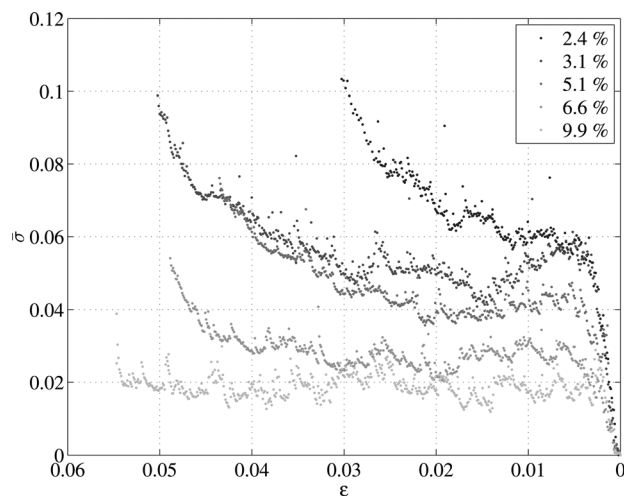

Fig. 5 Force-displacement response of five cylinders tested as per the schematic in Fig. 4(*b*). Before recording data, each is nominally compressed so that buckles form everywhere, and some manual adjustment is required to ensure an evenly distributed pattern. The axial load is then decreased to zero while measuring the end displacement, so the data proceed from left to right: at zero load, the displacement is set to be zero, and all values referred to this datum. The cylinders have initial radii, R_2, of 51.2, 51.8, 52.5, 53.3, and 55.0 mm, length l of 322, 326, 330, 335, and 345 mm, and all have the same thickness, $t = 0.044$ mm, giving a radius-to-thickness range of 1164–1250. The inner mandrel has a radius R_1 of 50 mm, so that initial mismatch strains, ξ, are equal to 2.4, 3.7, 5.1, 6.6, and 9.9%, respectively, as stated in the legend. The axial strain, ε, is the end-wise displacement divided by the initial height, and the axial stress, $\bar{\sigma}$, is found by dividing the axial force by the area of contact, $2\pi R_2 t$, and then again by the value of the classical axial buckling stress for a cylinder, $Et/(R_2\sqrt{3(1-\nu^2)})$, where E is the Young's modulus (4905 MPa) and ν is the Poisson's ratio (0.34) of Mylar.

higher friction, and it is energetically more favorable for the cylinder to offload one ring at a time. For the other three intermediate mismatch values, the axial response is a proportionate combination of these. For the next smallest mismatch, there is some progressive unloading at first, usually at one end but not necessarily so, until the general level of contact is small enough to favor overall sliding.

All of the force data is normalized by dividing by the material area of the cross section, to yield a stress quantity, which is then divided by the classical value of buckling stress for a perfect, stress-free cylinder, given by $Et/(R_2\sqrt{3[1-\nu^2]})$ [5], where E and ν are the Young's modulus (4905 MPa) and Poisson's ratio (0.34) of Mylar, and R_2 and t are the radius and thickness of the cylinder (R_1 is used later for the mandrel). We assume that our cylinders have buckled at the point when the force-displacement curves become nonlinear close to zero displacement, and in all cases, the equivalent stress is less than 0.06 times the classical value. Although Horton and Durham [1] were able to match the classical value, we expect a much lower load for two reasons known to detract from the buckling capacity. Our cylinders are unloaded, and we cannot guarantee a perfectly cylindrical form at the point where linearity is recovered. Second, the shell is not free of elastic stresses because wrapping a flat sheet introduces circumferential and axial bending moment distributions, and associated residual, sometimes compressive stresses.

In terms of the buckled shape, the number of diamonds remains fixed for each cylinder, their width varies imperceptibly and only their height changes during end-wise compression. Accordingly, the circumferential wavelength remains approximately constant, so this characteristic is equally defined by the number of circumferential diamonds. Figure 6 records this number, denoted as n, which is averaged over several axial positions for the Instron-tested cases, along with data from informal hand-held tests. These are plotted against the degree of initial mismatch, ξ, which is defined to be $R_2/R_1 - 1$ in the sense of a circumferential strain, and there is a clear, bounded trend in which n increases for decreasing ξ. The variation of the height of diamonds, h, with axial strain, ϵ, is displayed in Fig. 7. Measuring h is performed digitally from photographs of rings of diamonds at the top, middle, and bottom of the cylinder, before taking an average value across all of them. ϵ is the average strain given by the ratio of
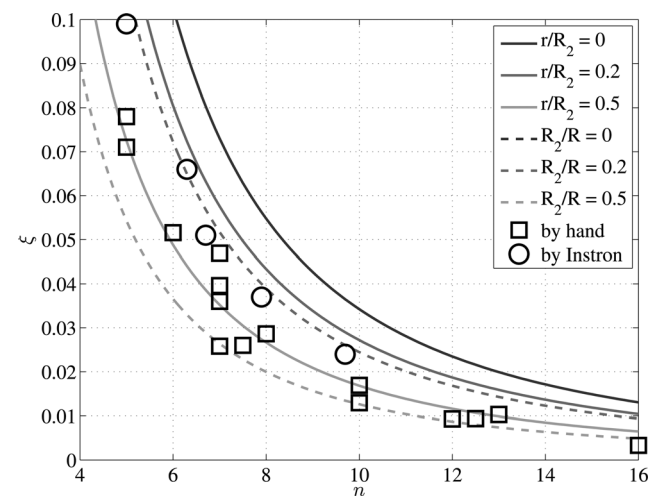
Fig. 6 Initial mismatch between the cylinder and mandrel, $\xi = R_2/R_1 - 1$, versus the number of circumferential buckles, n, in the postbuckling regime. The circles are obtained from the five Instron-tested cases in Fig. 5, where n is calculated by averaging their number on several axial levels. The squares apply to those manually compressed by hand on different mandrels (of radii 29.6, 31.6, and 63.5 mm), where n is averaged on two circumferences. Solid lines are predictions by Eq. (1) and Fig. 8(*b*), and dashed lines are predictions by Eq. (3) and Fig. 8(*c*).
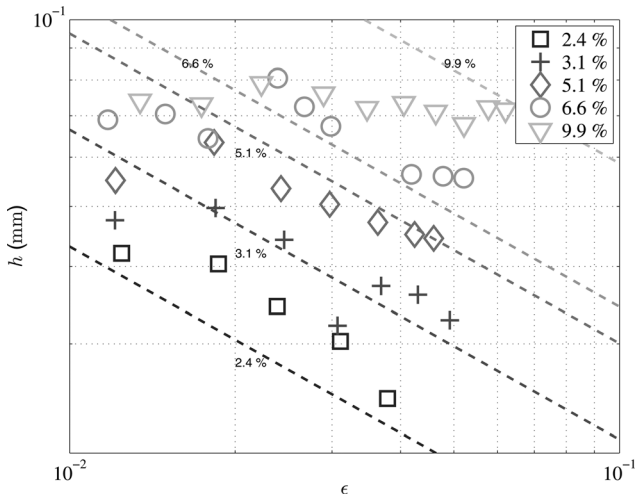
Fig. 7 Average buckle height, *h*, (Fig. 8) versus axial compressive strain, ϵ, for the five Instron-tested cases from Fig. 5 The extra lines are predictions by Eq. (4), which uses *n* from Fig. 6 All have the same gradient of $1/\sqrt{\epsilon}$, their mismatch strains are indicated alongside, and their colors match the legend symbols. Note that, generally, when the mismatch strain is smallest, all buckles deform in unison, and *h* is approximately governed by $1/\sqrt{\epsilon}$. As the mismatch increases, buckles tend to form progressively rather than together, so that some of the buckles have roughly constant height.

end-wise displacement to initial axial length. Plotting the variation on logarithmic axes reveals that there is, potentially, a power-law relationship but that this applies to the data in "clusters." As the mismatch becomes smaller, this relationship applies more uniformly across the data, but for larger mismatches, only part of the data conforms, otherwise it is generally flat, signifying that the height remains constant. The reason for this is due to whether or not the cylinder unloads progressively. When it does, the buckle height at all three axial positions cannot change simultaneously, and locally, only when the ring of buckles has opened up. When clusters conform to the power law, then all positions are

associated with rings that have already opened, which continue to offload. Note that all measurements are performed well beyond the nominal buckling limit, even for small strains.

3 Analysis

Figure 8 indicates a simple model for estimating the properties of the diamond buckles. Since the number of circumferential buckles does not depend on load, we can treat this separately from the height of buckles. Consider a circumferential line bisecting a given ring of diamond buckles, highlighted in Fig. 8(*a*). Assuming inextensible behavior, the length of this line is equal to the original cylindrical circumference, $2\pi R_2$, and takes one of two polygonal forms of *n* sides. In Fig. 8(*b*), the polygon has straight edges inspired by the Yoshimura pattern but interconnected by small rounded corners of uniform radius, *r*, to account for the finite size of adjacent creases. The center of all straight sides just touches the mandrel, of radius R_1. The form in Fig. 8(*c*) has instead uniformly curved sides to reflect those buckles which mostly adhere over the mandrel. So that we avoid having to specify a complex pattern with, for example, oppositely curved regions, the radius of the sides is set equal to $R > R_1$, and all sides are interconnected by zero-width vertices. Both of these generic forms are evident in the close-up detail in Fig. 2.
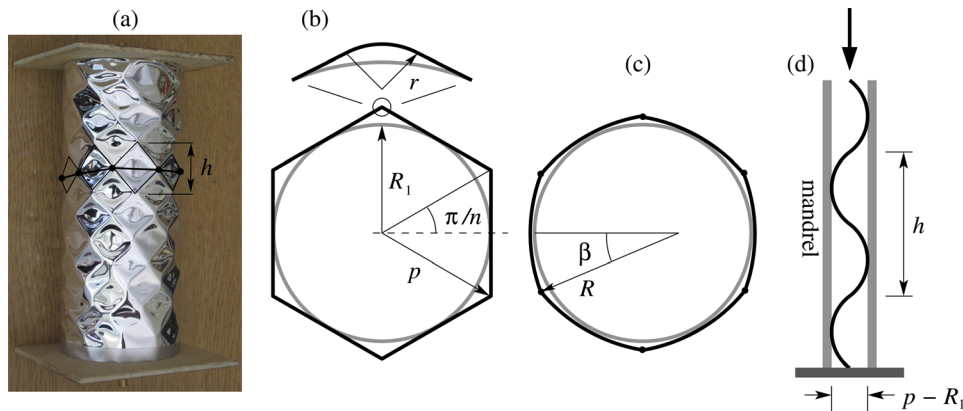
The angle subtended by *r* in Fig. 8(*b*) is $2\pi/n$, and each straight side has length $2(R_1 - r)\tan(\pi/n)$. A balance of circumferential lengths reveals

$$n[r2\pi/n + 2(R_1 - r)\tan(\pi/n)] = 2\pi R_2 \Rightarrow \frac{r}{R_2}$$
$$= \frac{(R_1/R_2)\tan(\pi/n) - \pi/n}{\tan(\pi/n) - \pi/n}$$

Recalling that $\xi = R_2/R_1 - 1$, the above may be expressed as

$$\xi_1 = \frac{\tan(\pi/n)}{\pi/n + (r/R_2)[\tan(\pi/n) - \pi/n]} - 1 \qquad (1)$$

after setting ξ equal to ξ_1 for this first case. Note that this reduces to

Fig. 8 Schematic details for estimating the buckled geometry. (*a*) The number of facets, *n*, on a given circumference is given by the number of diamond features touching on adjacent corners. (*b*) Simplified polygonal description of the circumferential path in (*a*) with *n* straight sides interconnected by a small regions of constant radius of curvature, *r*. When *r* is zero, the maximum radial distance from the center is *p* equal to $R_1/\cos(\pi/n)$. (*c*) The path is now described by *n* curved buckles of radius, *R*, subtending angle, 2β, but meeting discontinuously at points of infinite curvature. (*d*) Scheme for estimating the axial height, *h*, of buckles in which the edge is treated as a rod buckling between the inner mandrel and a fictitious outer constraint defined by the largest radial displacement, *p*, from (*b*). The axial displacement for a given facet is δ and the inner mandrel has radius, R_1.

$$\xi_1 = \frac{\tan(\pi/n)}{\pi/n} - 1 \qquad (2)$$

when r is zero. In Fig. 8(c), the circular sector formed by a single side subtends the semiangle β, equal to $\pi R_2/nR$ when inextensible. Using similar triangles within the sector, we may state

$$\frac{R\sin\beta}{R_1\sin(\pi/n)} = \frac{R_1 - R + R\cos\beta}{R_1\cos(\pi/n)} \Rightarrow \frac{R_1}{R_2}$$

$$= \frac{\pi}{n\beta}\left[\frac{\sin\beta}{\tan(\pi/n)} + 1 - \cos\beta\right]$$

and for the same definition of mismatch but denoting as ξ_2 for this second case, it can be shown

$$\xi_2 = \frac{\beta n/\pi}{1 - \cos\beta + (\sin\beta)/\tan(\pi/n)} - 1 \qquad (3)$$

It is not possible to solve explicitly for n, so we specify n and calculate ξ for given values of r and R. We note that both r and the curvature, $1/R$, are small in practice, and it makes sense to set them equal to fixed proportions of R_2 and $1/R_2$, respectively, which implies the same proportion of $\beta/(\pi/n)$ for calculating ξ_2. When both ratios are zero, then we have a single upper bound, Eq. (2), corresponding to a true polygon, and this is plotted in Fig. 6. Additional values of r/R_2 and R_2/R are chosen to be 0.2 and 0.5, arbitrarily, and ξ_1 and ξ_2 are calculated and added to the figure. The upper bound naturally overestimates the mismatch for a given n because of its simplicity, but the same downward trend is clearly evinced. The other two values predict curves that better fit the data with ξ_1 diverging at a slower rate compared to ξ_2 when the ratio increases.

The axial height of buckles may be estimated from Fig. 8(d), which interprets the deformed side profile of the cylinder as an axial rod undergoing planar buckling between rigid vertical constraints. One of them is the mandrel surface, and the other is foisted geometrically by considering the largest possible amplitude of buckle in the radial direction. This is related to the vertex distance p in Fig. 8(b), which is largest when r is zero, resulting in $p = R_1/\cos(\pi/n)$ and a radial buckling gap of $p - R_1$ in Fig. 8(d). For an inextensible rod with a sinusoidal profile, elementary geometry gives

$$\frac{\delta}{l} = \frac{\pi^2}{4}\left(\frac{\lambda}{l}\right)^2$$

where l is the half-wavelength, equal to $h/2$, and $\lambda = (p - R_1)/2$ is the amplitude. Recognize that δ/l is equivalent to the axial strain, ϵ, when δ is the change in axial length over a single buckled wavelength. Thus, we see

$$\epsilon = \frac{\pi^2}{4}\frac{(p - R_1)^2}{4}\frac{4}{h^2} \Rightarrow h = \frac{\pi R_1}{2\sqrt{\epsilon}}\left(\frac{1}{\cos(\pi/n)} - 1\right) \qquad (4)$$

Using experimental values of n from Fig. 6, this relationship is plotted on logarithmic axes in Fig. 7, where the power-law relationship of $1/\sqrt{\epsilon}$ manifests as straight lines of slope -0.5. Compared to the experimental data, the predicted heights are rather promising in that their absolute values are not too dissimilar, and rather good for the intermediate values of mismatch. The power-law trend is clear except for the largest mismatch even though the model is rather simple and given the difficulties encountered during testing. In all cases, the data for the smallest strain diverges from this relationship as the facets begin to disappear altogether, when the constraint effect is minimal and the model is least effective.

4 Conclusions and Discussion

Horton and Durham [1] were interested in verifying the classical buckling load by ensuring that imperfections were minimized while enabling the mode-shape to fully develop over its surface by means of a mandrel. Our buckling limits are rather lower, because we do not pay much attention to ensuring a perfectly cylindrical form initially. Instead, we compress the cylinders to some nominal value, manually adjust the buckling pattern to give a uniform mode-shape, before unloading to zero force, where our focus has been on the shape of individual buckles. The number of circumferential buckles, n, is set by the sizes of the cylinder and mandrel and not by the thickness of shell. The wavelength, or height, h, of axial buckles is governed by n indirectly, but is primarily set by the amount of end-wise compression. Because of large displacements, we are able to treat the deformation in terms of curving displacements alone, and simple but effective estimates of n and h have been garnered using approximate waveforms separately contrived in both directions.

We have deliberately avoided solving governing equations of deformation in pursuit of the simple formulas given by Eqs. (2) and (4). But there are other reasons, most notably, because we are working well within the postbuckling regime, where displacements are significant, and crucially, because we need to be able to incorporate the effect of the mandrel in a meaningful way. A linear stability analysis is, essentially, an eigenvalue solution in which the amplitude of displacement is indeterminate, so there is no way of accounting for the mandrel dimensions. A Koiter's circle approach [5] can provide information about the buckle size in the sense of respective wave numbers, but it too follows from the eigensolution, and it is a relative specification, in that one of the wave numbers is needed to define the other, as adopted by Hunt et al. [4], within a family of possible solutions. On the other hand, postbuckling analysis of the wrinkling of thin films has garnered recent momentum, where various authors propose appropriate displacement fields for describing their deformed shape and field profile. Most studies pursue an energy formulation with multiple components expressed as nonlinear functions of a particular deformation parameter. After minimization, a natural length for this parameter becomes apparent. This type of approach is not amenable here for establishing the circumferential wavelength, because the mandrel presents a rigid constraint, as noted in Sec. 1. However, connecting a wrapped sheet to a compliant core such as a sponge foam is not inconceivable, where axial compression may induce surface patterns similar to here. We are currently devising a simple physical demonstrator of this, but we note, in closing, that a possible hint at performance may be gleaned from the recent analytical work of [14] on the formation of texture along the internal walls of a cylindrical gut during differential growth where, again, different mode-shapes and patterns can emerge.

References

[1] Horton, W. H., and Durham, S. C., 1965, "Imperfections, A Main Contributor to Scatter in Experimental Values of Buckling Load," Int. J. Solids and Struct., **1**, pp. 59–72.

[2] Hutchinson, J. W., 2010, "Knockdown Factors for Buckling of Cylindrical and Spherical Shells Subject to Reduced Biaxial Membrane Stress," Int. J. Solids and Struct., **47**, pp. 1443–1448.

[3] Mandal, P. R., and Calladine, C. R., 2000, "Buckling of Thin Cylindrical Shells Under Axial Compression," Int. J. Solids and Struct., **37**, pp. 4509–4525.

[4] Hunt, G. W., Lord, G. J., and Petelier, M. A., 2003, "Cylindrical Shell Buckling: A Characterization of Localization and Periodicity," Discrete and Continuous Dynamical Systems—Series B, **3**(4), pp. 505–518.

[5] Calladine, C. R., 1983, Theory of Shell Structures, Cambridge University Press, Cambridge, UK.

[6] Hunt, G. W., and Ario, I., 2005, "Twist Buckling and the Foldable Cylinder: An Exercise in Origami," Int. J. Non-Linear Mech., **40**(6), pp. 833–843.

[7] Cai, S., Breid, D., Crosby, A. J., Suo, Z., and Hutchinson, J. W., 2011, "Periodic Patterns and Energy States of Buckled Films on Compliant Substrates," J. Mech. Phys. Solids, **59**, pp. 1094–1114.

[8] Mahadevan, L., and Rica, S., 2005, "Self-Organised Origami," Science, **307**, p. 1740.

[9] Audoly, B., and Boudaoud, A., 2008, "Buckling of a Thin Film Bound to a Compliant Substrate (Part 1). Formulation, Linear Stability of Cylindrical Patterns, Secondary Bifurcations," J. Mech. Phys. Solids, **56**(7), pp. 2401–2421.

[10] Hure, J., Roman, B., and Bico, J., 2012, "Stamping and Wrinkling of Elastic Plates," Phys. Rev. Lett., **109**, p. 054302.

[11] Mansfield, E. H., 1989, *The Bending and Stretching of Plates*, Cambridge University Press, Cambridge, UK.

[12] Johnson, W., Soden, P. D., and Al-Hassani, S. T. S., 1977, "Inextensional Collapse of Thin-Walled Tubes Under Axial Compression," IMechE J. Strain Analysis, **12**(4), pp. 317–339.

[13] Guest, S. D., and Pellegrino, S., 1994, "The Folding of Triangulated Cylinders, Part II: The Folding Process," ASME J. Appl. Mech., **61**, pp. 777–783.

[14] Shyer, A., Tallinen, T., Nerurkar, N., Wei, Z., Kim, E., Kaplan, D., Tabin, C., Mahadevan, L., 2013, "Villification: How the Gut gets Its Villi," Science, **342**, pp. 212–218.